PAPER • OPEN ACCESS

Mapping the complex refractive index of single layer graphene on semiconductor or polymeric substrates at terahertz frequencies

To cite this article: Valentino Pistore *et al* 2022 *2D Mater.* **9** 025018

IOP Publishing 2D Mater. 9 (2022) 025018 https://doi.org/10.1088/2053-1583/ac57c9

2D Materials

CrossMark

OPEN ACCESS

RECEIVED
2 January 2022

REVISED
15 February 2022

ACCEPTED FOR PUBLICATION
23 February 2022

PUBLISHED
16 March 2022

PAPER

Mapping the complex refractive index of single layer graphene on semiconductor or polymeric substrates at terahertz frequencies

Valentino Pistore[1], Osman Balci[2], Jincan Zhang[2], Sachin M Schinde[2], Adil Meersha[2], Andrea C Ferrari[2] and Miriam S Vitiello[1]

[1] NEST, CNR—Istituto Nanoscienze and Scuola Normale Superiore, Piazza San Silvestro 12, 56127 Pisa, Italy
[2] Cambridge Graphene Centre, University of Cambridge, Cambridge CB3 0FA, United Kingdom

E-mail: miriam.vitiello@sns.it

Keywords: refractive index, graphene, optical properties, terahertz

Supplementary material for this article is available online

Abstract

Assessing experimentally the main optical parameters of graphene (e.g. complex refractive index, carrier density, mobility) in the far-infrared (0.1–10 THz) is important for quantum science, due to the possibility to devise miniaturized devices (frequency combs, random lasers), components (optical switches, spatial light modulators, metamaterial mirrors and modulators) or photonic circuits, in which graphene can be integrated with existing semiconductor technologies to manipulate their optical properties and induce novel functionalities. Here, we combine time domain terahertz (THz) spectroscopy and Fourier transform infrared spectroscopy to extract the complex refractive index of large ($\sim$1cm^2) area single layer graphene on thin ($\sim$0.1-1 μm) polymeric suspended substrates, flexible and transparent films, and high reflectivity Si substrates in the 0.4–1.8 THz range. We model our data to extract the relevant optical (refractive index, absorption coefficient, penetration length) electronic (Fermi velocity) and electrical (carrier density, mobility) properties of the different graphene samples.

1. Introduction

The mechanical [1], thermal [2, 3], electronic [4] and optical properties [5] of single layer graphene (SLG) have been thoroughly investigated [6]. Its excellent transport and optical characteristics and its atomic layer thickness can be exploited to develop novel device architectures, such as flexible electronic devices with high (up to 10^{5}cm^2/Vs) mobilities [7], spintronic devices [8], broadband optical modulators [9] and super-capacitors for energy storage [10], among others [11–13] Its ultra-high mobility (70000 cm^2/Vs at room temperature and 120000 cm^2/Vs at 9K)[14] is attractive for the realization of opto-electronic and photonic devices across the infrared [15–17]. In the terahertz (THz) (0.1–10 THz) or far-infrared (0.3–30 THz), graphene was used to prepare emitters [18], photo-detectors [19] and modulators [20, 21, 22, 23]. Engineering graphene- or hybrid semiconductor-graphene-photonic devices requires a precise knowledge of its core optical parameters. While SLG has been widely investigated in the visible (380–750 nm) [5] and near infrared (780–2500 nm) [24], a detailed determination of its substrate-dependent [25–28] optical properties at THz frequencies is still lacking and has not been performed on substrates which can be fundamental to THz technologies, such as polycarbonate (PC) [29] and polymethylmethacrylate (PMMA) [29].

Large ($\sim$1cm^2) area chemical vapor deposition (CVD) graphene on flexible and transparent films is promising for optoelectronic applications for wearable devices in the visible and IR [6, 15, 30, 31]. This also raises the interest into the fundamental optical properties of large area SLG deposited onto polymers such as PC and PMMA .

The most commonly adopted technique to probe the optical response of materials to THz radiation is time-domain spectroscopy [32] (THz-TDS), which provides detailed information with sub-ps resolution [33]. The optical properties of SLG and multi-layer graphene on many different substrates were previously investigated by THz-TDS [28, 34–40] to retrieve the complex optical conductivity, a key parameter to determine other fundamental properties, such as carrier density, scattering time, mobility and refractive index. The real and imaginary part of the refractive index of SLG on SiO_2/Si, to the best of our knowledge, has been only reported in the sub-THz range [41], but not supported by information about the used SLG morphological, structural and optical properties. A systematic study, comprehensive of a complete SLG characterization, is therefore necessary.

Here we report the frequency dependent complex refractive index of SLG grown by CVD and transferred on PC, PMMA and a 500 μm thick, high resistivity (HR, ∼10 kΩ × μm), double side polished Si with 285 nm SiO_2 on both sides. We use a combination of THz-TDS, for 0.4–1.8 THz, and Fourier transform infrared spectroscopy (FTIR), for 1.5–20 THz, to extract the relevant optical (refractive index, absorption coefficient, penetration length), electronic (Fermi velocity) and electrical (carrier density, mobility) properties of the different graphene samples across the THz frequency range.

2. Materials and methods

We use three SLG samples grown by CVD on Cu. These are then transferred by electrochemical delamination in a 1 M NaOH aqueous solution. The 1st substrate (A) is 500 μm, double side polished, slightly doped (resistivity ∼10 kΩ × μm) HR Si with 285 nm SiO_2 on both sides. The 2nd (B) and the 3rd (C) are 2.9 ± 0.1 μm thick PC and 166 ± 25 nm thick PMMA, spin coated on SLG/Cu as the supporting layer for SLG transfer. SLG/PC and SLG/PMMA with 1.6 ± 0.1 μm and 229 ± 27 nm thickness are suspended onto a frame of ∼100 μm thick polyvinyl chloride with 1.2 cm × 1.2 cm holes at the centre (figure 1(a)). Identical substrates without SLG are used as a reference. Optical images of the three samples, with SEM and AFM images of sample A, are reported in the supplementary information (available online at stacks.iop.org/TDM/9/025018/mmedia). All thicknesses are measured with a Stylus Profilometer (DEKTAK XT from Bruker).

As grown and transferred SLG are characterized by Raman spectroscopy with a Renishaw InVia Raman spectrometer equipped with a 100× objective at 514.5 nm, with power on the sample <0.5 mW to exclude heating effects. An analysis of three spectra on as grown SLG on Cu, seven on transferred SLG on SiO_2/Si, six on transferred SLG on PC and six on transferred SLG on PMMA is performed to estimate doping, strain, and defect density. The errors are calculated from the standard deviation across different spectra, the spectrometer resolution (∼1 cm^{-1}) and the uncertainty associated with the different methods to estimate doping and strain.

Figure 1(b) plots the Raman Spectrum of SLG on Cu after Cu photoluminescence removal [42]. The 2D peak is a single Lorentzian with FWHM(2D) ∼23 ± 1 cm^{-1}, signature of SLG [43]. The position of the G peak, Pos(G), is 1585 ± 2 cm^{-1}, with FWHM(G) ∼16 ± 2 cm^{-1}. The 2D peak position, Pos(2D), is 2703 ± 4 cm^{-1}, while the 2D to G peak intensity and area ratios, I(2D)/I(G) and A(2D)/A(G), are ∼3.7 ± 0.4 and 5.6 ± 0.9. No D peak is observed, indicating negligible Raman active defects in as grown SLG [44, 45]. The Raman spectrum of SLG on SiO_2/Si is in figure 1(b). The 2D peak retains its single-Lorentzian line shape with FWHM(2D) ∼28 ± 2 cm^{-1}. Pos(G) ∼1592 ± 2 cm^{-1}, FWHM(G) ∼9 ± 1 cm^{-1}, Pos(2D) ∼2691 ± 3 cm^{-1}, I(2D)/I(G) ∼1.6 ± 0.1 and A(2D)/A(G) ∼4.7 ± 0.2 indicating a p doping with Fermi energy E_F ∼300 ± 50 meV [46], which corresponds to a carrier concentration n ∼5.6 ± 1.5 × 10^{12} cm^{-2} [47, 48]. I(D)/I(G) ∼0.01 ± 0.01 corresponds to a defect density n_D ∼2.6 ± 1.5 × 10^9 cm^{-2} [46] for excitation energy 2.41 eV and E_F = 300 ± 50 meV. The Raman spectrum of SLG on PC is in figure 1(b). The 2D peak retains its single-Lorentzian line shape with FWHM(2D) ∼33 ± 1 cm^{-1}, Pos(G) ∼1593 ± 1 cm^{-1}, FWHM(G) ∼14 ± 1 cm^{-1}, Pos(2D) ∼2696 ± 2 cm^{-1}, I(2D)/I(G) ∼3.2 ± 0.5 and A(2D)/A(G) ∼7.8 ± 1.5 indicating a p doping with E_F ∼130 ± 60 meV [46], which corresponds to n ∼1.1 ± 0.9 × 10^{12} cm^{-2} [47, 48]. I(D)/I(G) ∼0.03 ± 0.02 implies n_D ∼8.3 ± 3.1 × 10^9 cm^{-2} [46] for 2.41 eV and E_F ∼130 ± 60 meV. The Raman spectrum of SLG transferred on PMMA is in figure 1(b). The 2D peak retains its single-Lorentzian line shape with FWHM(2D) ∼32 ± 2 cm^{-1}, Pos(G) ∼1589 ± 2 cm^{-1}, FWHM(G) ∼16 ± 1 cm^{-1}, Pos(2D) ∼2691 ± 2 cm^{-1}, I(2D)/I(G) ∼4.1 ± 0.7 and A(2D)/A(G) ∼8.2 ± 1.4 indicating a p doping with E_F ∼140 ± 30 meV [46], which corresponds to n ∼1.3 ± 0.4 × 10^{12} cm^{-2} [47, 48]. I(D)/I(G) ∼0.04 ± 0.07 indicates n_D ∼1.4 ± 0.7 × 10^{10} cm^{-2} [46] for 2.41 eV and E_F ∼140 ± 30 meV. Pos(G) and Pos(2D) are also affected by the presence of strain. For uniaxial (biaxial) strain, Pos(G) shifts by ΔPos(G)/$\Delta\varepsilon$ ∼23(60) cm^{-1}/% [49–51]. Pos(G) also depends on doping [47]. The average doping as derived from A(2D)/A(G), FWHM(G), I(2D)/I(G) should correspond to Pos(G) ∼1593 ± 2 cm^{-1} on SiO_2, ∼1584 ± 1 cm^{-1} on PC, ∼1584 ± 1 cm^{-1} on PMMA for unstrained SLG [47, 48]. However, we have Pos(G) ∼1592 ± 2 cm^{-1} on SiO_2, Pos(G) ∼1593 ± 1 cm^{-1} on PC, Pos(G) ∼1589 ± 2 cm^{-1} on PMMA which implies a contribution from uniaxial (biaxial) strain 0.02% ± 0.03% (0.05% ± 0.07%) on SiO_2, 0.14% ± 0.01% (0.38% ± 0.04%) on

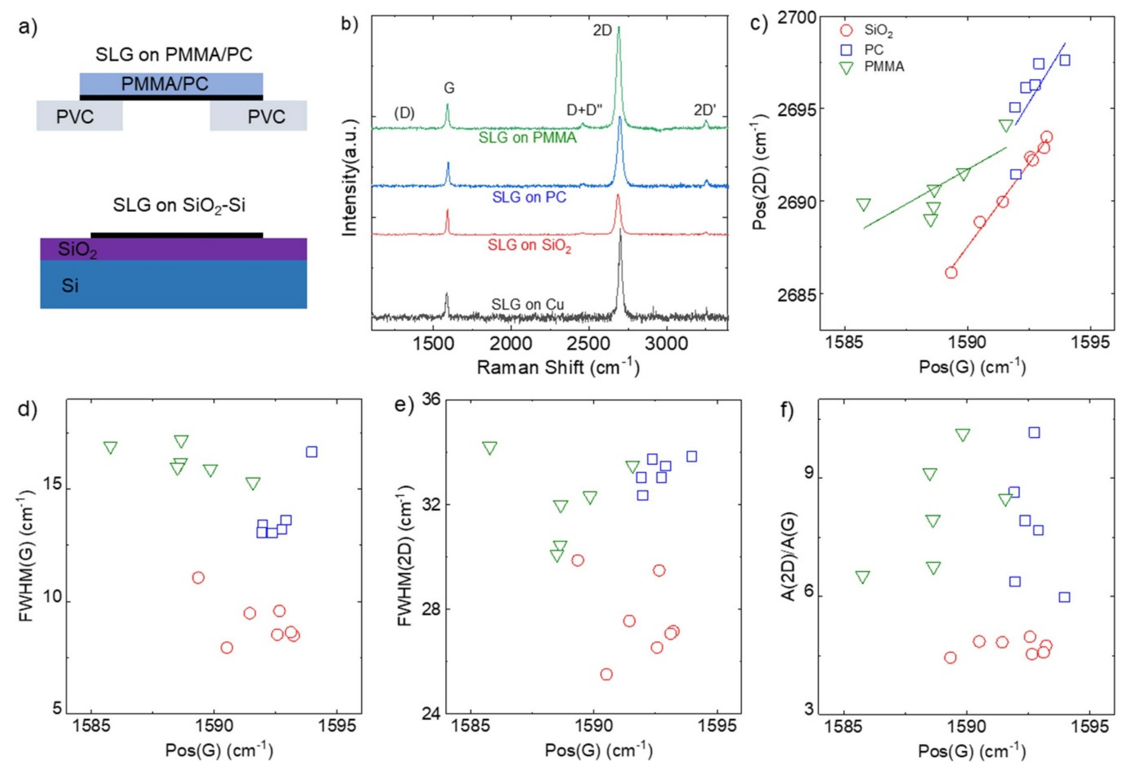

Figure 1. (a) Schematic of SLG on PC, PMMA and Si/SiO_2. (b) Representative Raman spectra of SLG on Cu, SiO_2, PC, PMMA. (c) Pos(2D) as a function of Pos(G) with linear fitting for each substrate. (d) FWHM(G) as a function of Pos(G). (e) FWHM(2D) as a function of Pos(G). (f) A(2D)/A(G) as a function of Pos(G).

PC, 0.08% ± 0.04% (0.20% ± 0.10%) on PMMA [49–51]. Local variations in strain and doping manifest as a spread in Pos(G) and Pos(2D), which in our samples vary between ∼1589–1593 cm^{-1} and ∼2686–2694 cm^{-1} on SiO_2, ∼1592–1594 and ∼2691–2698 cm^{-1} on PC, ∼1586–1592 and ∼2689–2694 cm^{-1} on PMMA (figures 1(d)–(f)). In presence of uni-axial (biaxial) strain, and in the absence of doping, ΔPos(2D)/ΔPos(G) ∼2.5 [49, 50, 52]. In our samples ΔPos(2D)/ΔPos(G) ∼1.8 ± 0.1 on SiO_2, ΔPos(2D)/ΔPos(G) ∼2.2 ± 1.0 on PC, ΔPos(2D)/ΔPos(G) ∼0.8 ± 0.3 on PMMA which indicates that the variation of Pos(G) is due to both doping and strain (figure 1(c)).

3. Results and discussion

Figure 2(a) plots three representative 800 ps time scans, corresponding to THz transmission through air (black), with Si reference (blue) and with sample A (red) collected with a THz TDS system in purged environment (Tera K5 by MenloSystems).

The inset is a zoom of the scans around the main pulse and the 1st three echoes related to the internal reflections. Each echo can be isolated from its neighbors, and contains the same information carried by the main pulse [53, 54]. Therefore, the latter can be employed to extract the complex transmittivity of the SLG [53, 54]. The electric field amplitude spectra obtained by windowing and then Fourier-transforming the first-pass of the THz pulse are in figure 2(b). The reduced spectral amplitude in sample A, compared to the reference, is due to the SLG intra-band absorption in the THz range [55]. An analogous procedure is followed for samples B, C.

The extrapolated TDS transmission spectrum is then compared with the sample transmittance directly measured under vacuum, via FTIR (Bruker, Vertex 80). As the FTIR lower frequency limit is 50 cm^{-1}, i.e. 1.5 THz, the two curves can be compared (figure 2(c)) to determine the upper frequency limit of our TDS measurements. This reveals that the transmittance extracted from THz-TDS diverges at ∼2 THz, meaning that the low amplitude of the THz electric field emitted by the antenna above that frequency significantly increases the uncertainty of the associated measurements. The same happens on the low frequency side, being the noise significant (SNR < 1) below 0.2 THz. Therefore, a conservative choice is to limit our analysis to the 0.4–1.8 THz range.

The FTIR transmittances of SLG onto PC (sample B) and PMMA (sample C) are shown in figure 2(c) (blue and green curves). These indicate a lower transparency at all frequencies compared to the Si case. This can be attributed to the thicker reference substrates than those used for SLG transfer, which introduce additional losses. The transport properties of

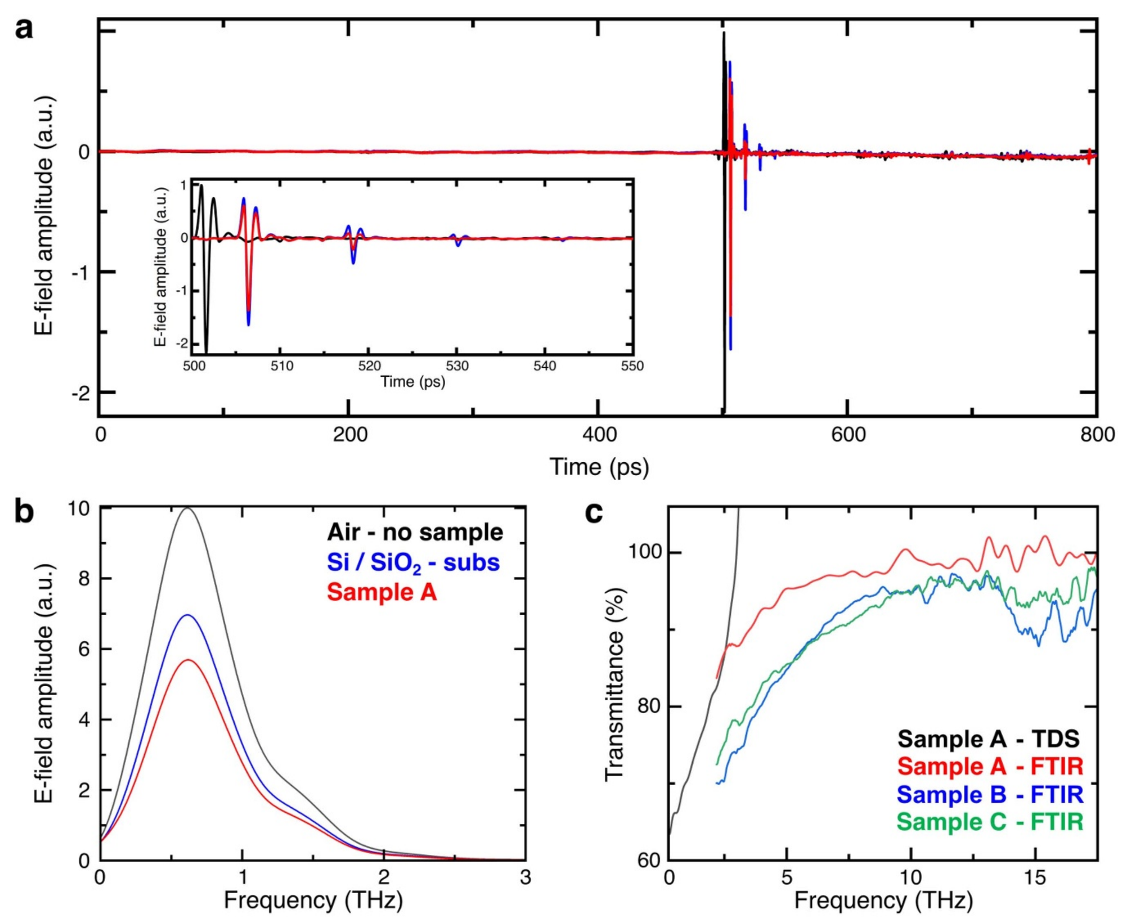

Figure 2. (a) THz-TDS time traces measured without sample (black), with Si reference (blue) and with SLG (red). Inset: zoom of the time traces around the transmitted pulses. (b) Spectra of the electric field associated with the main THz pulse of (a). (c) Comparison between SLG transmittance measured with THz-TDS (black) and with FTIR (red). The FTIR transmittances measured through SLG on PC (sample B) and PMMA (sample C) are in blue and green, respectively.

SLG are also affected by its interaction with the substrate through e.g. topographic corrugations [27], electron-density inhomogeneities [26] and interfacial phonon modes [25], which can also explain the different THz transmittance. Since the transmittance of samples B and C is still similar, we can expect to find the greatest difference in the optical conductivity between these two samples and sample A.

From the spectral amplitude ratio and phase difference of the Fourier-transformed time traces for sample A and the related reference (figure 2(a)), we retrieve the complex optical conductivity via the Tinkham formula [57]:

$$\tilde{\sigma}_{\mathrm{g}}(\omega) = \left\{\left[\tilde{n}_{\mathrm{Subs}}(\omega)+1\right]\left[1/\tilde{T}(\omega)-1\right]\right\}/Z_0 \quad (1)$$

where $\tilde{n}_{\mathrm{Subs}}(\omega)$ is the complex refractive index of the SiO_2 substrate [58], $\tilde{T}(\omega)=\tilde{E}_{\mathrm{g}}(\omega)/\tilde{E}_{\mathrm{Ref}}(\omega)$ is the complex transmittivity of SLG i.e. the ratio between the complex electric field spectra of SLG, $\tilde{E}_{\mathrm{g}}(\omega)$, and the reference, $\tilde{E}_{\mathrm{Ref}}(\omega)$. $Z_0 = 376.73\,\Omega$ is the impedance of free space.

We use a different approach to investigate the optical properties of SLG on PC and PMMA. The electric field time traces for samples B and C (figure 3(a)) show that echoes cannot be separated from the first-pass, since the time between internal reflections in the substrate is comparable with the pulse duration. The limited absorption occurring in the very thin (1.6 μm and 229 nm respectively) substrates of samples B and C introduces only small variations in the electric field amplitude of the transmitted pulses, which consequently appear very similar. The spectral amplitudes of the electric field (figure 3(b)) for bare and SLG-covered samples contain the information of all the multiple reflections of the THz radiation at the sample interfaces. Therefore, we need to account for the contributions of all internal reflections to the THz transmittivity, leading to a modified expression for the conductivity of SLG on an optically thin substrate [59]:

$$\tilde{\sigma}_{\mathrm{g}}(\omega) = \frac{\left\{\left[\tilde{n}_{\mathrm{Subs}}(\omega)+1\right]^2+\left[\tilde{n}_{\mathrm{Subs}}(\omega)-1\right]^2 \mathrm{e}^{-i\delta}\right\}}{\left\{\left[\tilde{n}_{\mathrm{Subs}}(\omega)+1\right]+\left[\tilde{n}_{\mathrm{Subs}}(\omega)-1\right]^2 \mathrm{e}^{-i\delta}\right\}} \times \frac{\left[1/\tilde{T}(\omega)-1\right]}{Z_0} \quad (2)$$

where $\delta = d_{\mathrm{Subs}} n_{\mathrm{Subs}} \omega / c$ is the phase shift between subsequent reflections, d_{Subs} the substrate thickness

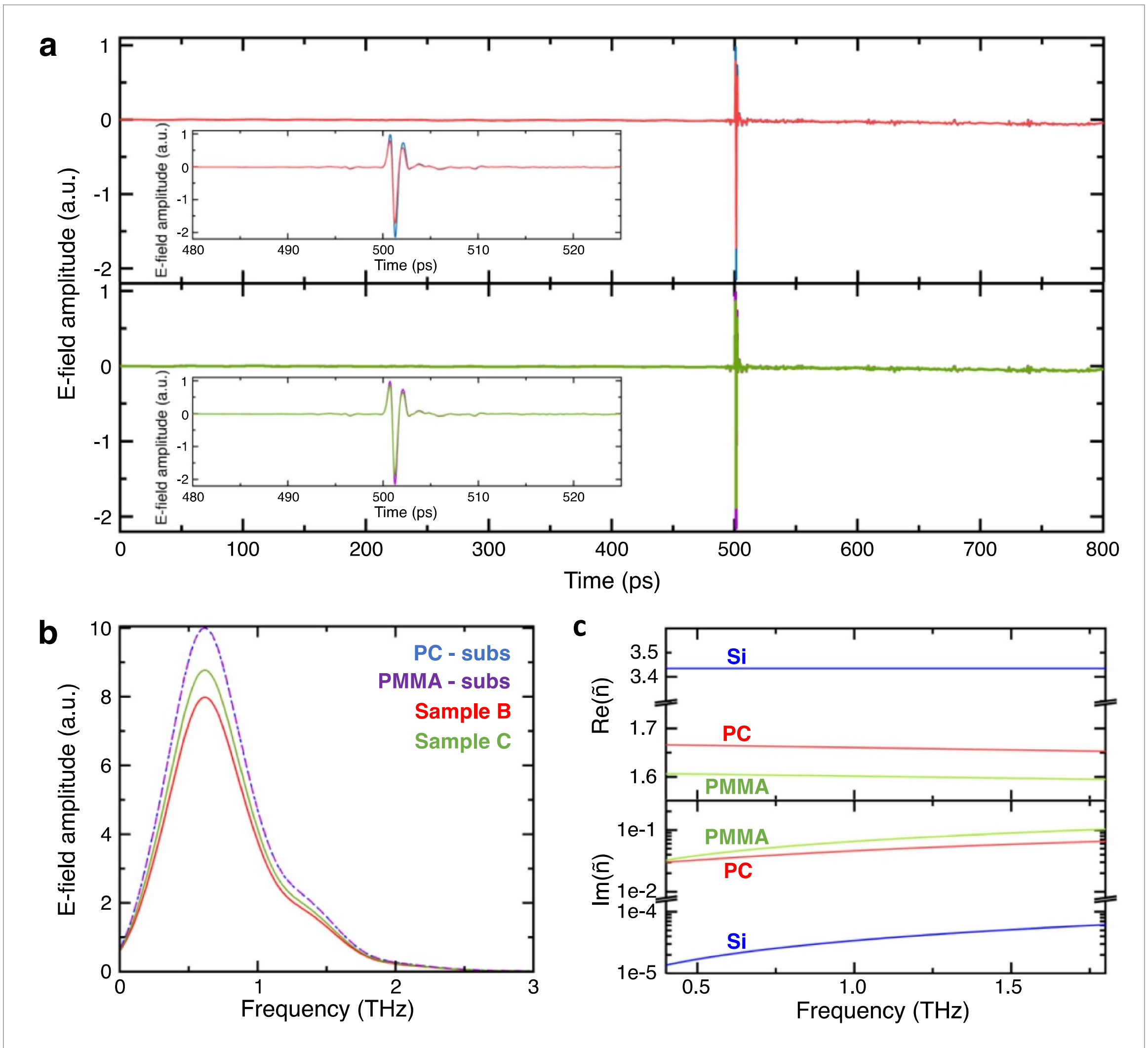

Figure 3. (a) Top panel: THz-TDS time traces for (blue) PC bare substrate and (red) SLG on PC (sample B). Bottom panel: THz-TDS time traces measured for (purple) PMMA bare substrate and (green) SLG on PMMA (sample C). (b) Spectra of electric field obtained by Fourier-transforming the time traces in (a). (c) Real (top panel) and imaginary (bottom panel) parts of the refractive indexes of HR-Si (blue curve), PC (red curve) and PMMA (green curve) as from [29, 56].

and n_{Subs} its refractive index. Since both references and samples B and C have different thicknesses, such a thickness discrepancy must be considered in the transmittivity amplitude and phase. The refractive indexes of the individual substrates in figure 3(c) are taken from Ref. [56] for high reflectivity silicon and from Ref. [29] for PC and PMMA.

The real (blue) and imaginary (orange) parts of the optical conductivity of SLG on different substrates is in figures 4(a)–(c) (solid lines) together with a Drude model fit [54, 60], then used to determine the scattering time, τ, and the DC sheet conductivity, σ_{DC}. We get σ_{DC} ~2.10 mS and τ ~103 fs for sample A, σ_{DC} ~1.50 mS and τ ~51 fs for sample B and σ_{DC} ~0.84 mS and τ ~58 fs for sample C. The Drude model well reproduces the experimental data, with an almost perfect agreement for thinner substrates. This is expected since the substrate contribution of the polymeric films to $\tilde{T}(\omega)$ is much lower than that associated with the thick Si substrate, hence reducing the errors related to substrate thickness determination or angular tilt [61].

The SLG complex permittivity $\tilde{\varepsilon}_{\mathrm{g}}(\omega)$ can then be obtained from:

$$\tilde{\varepsilon}_{\mathrm{g}}(\omega) = 1 - \frac{i\tilde{\sigma}_{\mathrm{g}}(\omega)}{(\omega\varepsilon_0 d_{\mathrm{g}})} \tag{3}$$

where ε_0 is the dielectric constant of vacuum and d_{g} is the SLG thickness, 0.335 nm [62]. Since $\mathrm{Re}\left[\tilde{n}_{\mathrm{g}}(\omega)\right] + i \times \mathrm{Im}\left[\tilde{n}_{\mathrm{g}}(\omega)\right] = \sqrt{\tilde{\varepsilon}_{\mathrm{g}}(\omega)}$, the SLG complex refractive index is then retrieved. Figures 4(d)–(f) displays the real (blue) and the imaginary (red) parts of the SLG refractive index with the corresponding Drude model fit (dashed lines). The SLG absorption coefficient and penetration depth are given by:

$$\mu_{\mathrm{a,g}}(\omega) = 2\frac{\Im\left[\tilde{n}_{\mathrm{g}}(\omega)\right]\omega}{c} \tag{4}$$

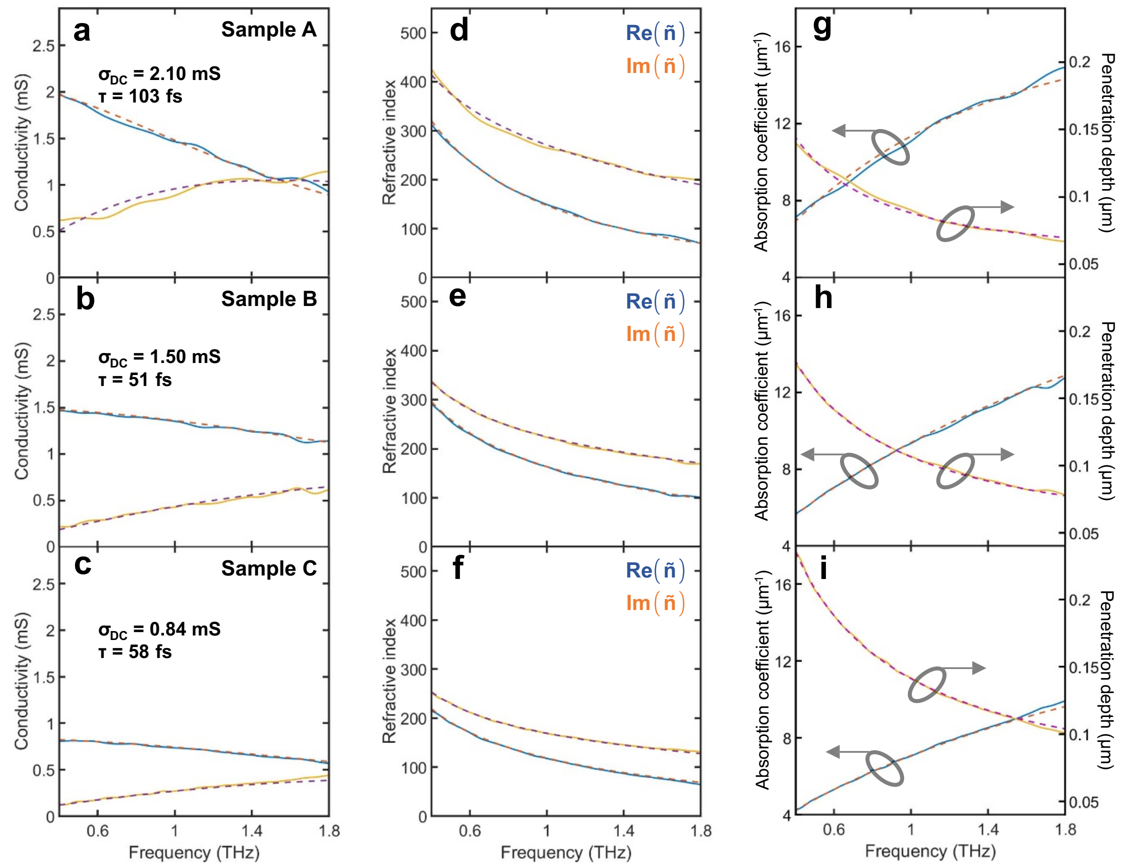

Figure 4. (a)–(c) Real (blue) and imaginary (orange) parts of the optical conductivity for samples (a) A (SLG on Si), (b) B (SLG on PC), (c) C (SLG on PMMA) (from top to bottom). Dashed lines represent the fitting with the Drude model. (d)–(f) Real (blue) and imaginary (orange) parts of the refractive index of samples (d) A, (e) B, (f) C, corresponding to the conductivities in (a)–(c). (g)–(i) Absorption coefficient (blue) and penetration depth (orange) for samples (g) A, (h) B, (i) C.

$$\delta_g = \frac{1}{\mu_{a,g}(\omega)} \quad (5)$$

displayed in figure 4(c), together with the corresponding fitting traces.

The complex refractive indexes show a similar behavior for samples B and C, both lower than sample A, with a smaller absolute decrease at higher frequencies, in agreement with the trend observed from the FTIR spectra. This also confirms that the SLG interaction with the substrate plays a key role in determining its optical properties at THz frequencies and must be taken into account in the design of SLG-based devices as, e.g. the absorption coefficient can change over factor 2 (see figures 1(g) and (i)) as a consequence of the electron-density inhomogeneities [26] and interfacial phonon modes [25], as confirmed by previous theoretical and experimental reports on SiO_2 [26, 63], Pt [64] and Cu [65] substrates.

The carrier density, mobility and Fermi velocity can also be derived from the optical conductivity. In order to account for electron–electron interactions, the Fermi velocity must be renormalized before extracting the other properties [40, 66]. We follow Ref. [40] to compute the renormalized Fermi velocity, together with carrier density and mobility. We use the relative permittivity of the substrate at 1 THz, which is a good approximation given the small dispersion of the refractive indexes of the substrate materials in the considered frequency range (figure 3(c)). The resulting renormalized Fermi velocity $v_F{}^*$, n, and mobility μ are in table 1.

The n values extracted from TDS measurements and Raman measurements show a discrepancy that ranges from 27% (sample C) to 73% (sample A). This is an effect of the renormalization of the Fermi velocity and of the dissimilar experimental conditions: while TDS experiments are performed in a purged controlled atmosphere, the Raman spectra are collected while keeping the samples in air, resulting in a different refractive index of the surrounding media.

The effect of the substrate onto the SLG electric characteristics was investigated in Ref. [28]. This showed that μ is mostly affected by n via substrate-induced charge doping, whereas τ is mostly unaffected by the substrate. Our findings confirm this conclusion as both sample B and C have similar $\tau = 51$ fs and $\tau = 58$ fs, yet the mobility changes by more than a factor 2 and the carrier concentration is

Table 1. Renormalized $v_F{}^*$, n_g and μ_g for samples A–C.

Sample	$v_F{}^*$	n	μ	n (Raman)
A	1.21×10^6 m s^{-1}	1.50×10^{12} cm^{-2}	8733 cm^2 V^{-1} s^{-1}	$5.6 \pm 1.5 \times 10^{12}$ cm^{-2}
B	1.22×10^6 m s^{-1}	3.07×10^{12} cm^{-2}	3050 cm^2 V^{-1} s^{-1}	$1.1 \pm 0.9 \times 10^{12}$ cm^{-2}
C	1.30×10^6 m s^{-1}	6.57×10^{11} cm^{-2}	7977 cm^2 V^{-1} s^{-1}	$1.3 \pm 0.4 \times 10^{12}$ cm^{-2}

$\sim$4.7 higher for sample B. n in sample C is a factor of 2.3 lower than A, in contrast with the significant (>2) increase reported in Ref. [28]. This can be at least in part attributed to the $V_F = 1.1 \times 10^6$ m s^{-1} used in Ref. [28], that did not consider the role of electron–electron interactions. In our case, using a constant $V_F = 1.1 \times 10^6$ m s^{-1} would have led to a 21% and 40% higher carrier density for samples A and C, respectively, than that obtained through the renormalization. This is particularly significant for substrates with low (<2.5) relative permittivity [40].

4. Conclusions

We reported the frequency dependent complex refractive index of SLG deposited on a thick (500 μm) HR SiO_2/Si and onto two thin (1.6 μm and 229 nm) polymeric films of PC and PMMA, in a frequency range 0.4–1.8 THz. Our experimental data allowed us to retrieve all relevant optical (refractive index, absorption coefficient, penetration length) electronic (Fermi velocity) and electrical (carrier density, mobility) properties of the different graphene samples, in the terahertz. Assessing experimentally the optical parameters for graphene layers on large ($\sim$1cm^2) area polymeric films is of interest for the development of graphene-based wearable optoelectronic or miniaturized quantum photonic devices, such as frequency combs [67] or low spatial coherence random lasers [68].

Data availability statement

The data that support the findings of this study are available upon reasonable request from the authors.

Acknowledgments

We acknowledge funding from the ERC Grants (681379) SPRINT, Hetero2D, GSYNCOR, EU Graphene Flagship, EPSRC Grants EP/L016087/1, EP/K01711X/1, EP/K017144/1, EP/N010345/1. We would like to thank Leonardo Viti for support with image acquisition.

Conflict of interest

The authors declare no conflict of interest.

ORCID iDs

Jincan Zhang https://orcid.org/0000-0002-7131-4491
Miriam S Vitiello https://orcid.org/0000-0002-4914-0421

References

[1] Papageorgiou D G, Kinloch I A and Young R J 2017 Mechanical properties of graphene and graphene-based nanocomposites *Prog. Mater. Sci.* **90** 75–127
[2] Pop E, Varshney V and Roy A K 2012 Thermal properties of graphene: fundamentals and applications *MRS Bull.* **37** 1273–81
[3] Kumar A, Sharma K and Dixit A R 2019 A review of the mechanical and thermal properties of graphene and its hybrid polymer nanocomposites for structural applications *J. Mater. Sci.* **54** 5992–6026
[4] Castro Neto A H, Guinea F, Peres N M R, Novoselov K S and Geim A K 2009 The electronic properties of graphene *Rev. Mod. Phys.* **81** 109–62
[5] Falkovsky L A 2008 Optical properties of graphene *J. Phys.: Conf. Ser.* **129** 012004
[6] Ferrari A C *et al* 2015 Science and technology roadmap for graphene, related two-dimensional crystals, and hybrid systems *Nanoscale* **7** 4598–810
[7] Chen J-H, Ishigami M, Jang C, Hines D, Fuhrer M and Williams E 2007 Printed graphene circuits *Adv. Mater.* **19** 3623–7
[8] Kamalakar M V, Groenveld C, Dankert A and Dash S P 2015 Long distance spin communication in chemical vapour deposited graphene *Nat. Commun.* **6** 6766
[9] Liu M, Yin X, Ulin-Avila E, Geng B, Zentgraf T, Ju L, Wang F and Zhang X 2011 A graphene-based broadband optical modulator *Nature* **474** 64–67
[10] El-Kady M F, Shao Y and Kaner R B 2016 Graphene for batteries, supercapacitors and beyond *Nat. Rev. Mater.* **1** 16033
[11] Yan H, Low T, Zhu W, Wu Y, Freitag M, Li X, Guinea F, Avouris P and Xia F 2013 Damping pathways of mid-infrared plasmons in graphene nanostructures *Nat. Photon.* **7** 394–9
[12] Park D-W *et al* 2014 Graphene-based carbon-layered electrode array technology for neural imaging and optogenetic applications *Nat. Commun.* **5** 5258
[13] Perreault F, de Faria A F and Elimelech M 2015 Environmental applications of graphene-based nanomaterials *Chem. Soc. Rev.* **44** 5861–96
[14] de Fazio D *et al* 2019 High-mobility, wet-transferred graphene grown by chemical vapor deposition *ACS Nano* **13** 8926–35
[15] Bonaccorso F, Sun Z, Hasan T and Ferrari A C 2010 Graphene photonics and optoelectronics *Nat. Photon.* **4** 611–22
[16] Koppens F H L, Mueller T, Avouris P, Ferrari A C, Vitiello M S and Polini M 2014 Photodetectors based on graphene, other two-dimensional materials and hybrid systems *Nat. Nanotechnol.* **9** 780–93

[17] Romagnoli M *et al* 2018 Graphene-based integrated photonics for next-generation datacom and telecom *Nat. Rev. Mater.* **3** 392–414
[18] Yadav D *et al* 2018 Terahertz light-emitting graphene-channel transistor toward single-mode lasing *Nanophotonics* **7** 741–52
[19] Liu J *et al* 2021 Recent progress in the development of graphene detector for terahertz detection *Sensors* **21** 4987
[20] Gaspare A D *et al* 2021 Tunable, grating-gated, graphene-on-polyimide terahertz modulators *Adv. Funct. Mater.* **31** 2008039
[21] Liu X, Jia M, Fan S, Stantchev R I, Chen X, Pickwell-Macpherson E and Sun Y 2021 Deep THz modulation at Fabry–Perot resonances using graphene in periodic microslits *Opt. Express* **29** 6199–208
[22] Hasan M, Arezoomandan S, Condori H and Sensale-Rodriguez B 2016 Graphene terahertz devices for communications applications *Terahertz Commun.* **10** 68–78
[23] Wang M and Yang E-H 2018 THz applications of 2D materials: graphene and beyond *Nano-Struct. Nano-Objects* **15** 107–13
[24] Hendry E, Hale P J, Moger J, Savchenko A K and Mikhailov S A 2010 Coherent nonlinear optical response of graphene *Phys. Rev. Lett.* **105** 097401
[25] Serov A Y, Ong Z-Y, Fischetti M V and Pop E 2014 Theoretical analysis of high-field transport in graphene on a substrate *J. Appl. Phys.* **116** 034507
[26] Zhang Y, Brar V W, Girit C, Zettl A and Crommie M F 2009 Origin of spatial charge inhomogeneity in graphene *Nat. Phys.* **5** 722–6
[27] Deng S and Berry V 2016 Wrinkled, rippled and crumpled graphene: an overview of formation mechanism, electronic properties, and applications *Mater. Today* **19** 197–212
[28] Kim J Y, Lee C, Bae S, Kim K S, Hong B H and Choi E J 2011 Far-infrared study of substrate-effect on large scale graphene *Appl. Phys. Lett.* **98** 201907
[29] Zhai M, Locquet A and Citrin D S 2020 Pulsed THz imaging for thickness characterization of plastic sheets *NDT&E Int.* **116** 102338
[30] Anagnostopoulos G *et al* 2016 Mechanical stability of flexible graphene-based displays *ACS Appl. Mater. Interfaces* **8** 22605–14
[31] Xie J, Chen Q, Shen H and Li G 2020 Review—wearable graphene devices for sensing *J. Electrochem. Soc.* **167** 037541
[32] Neu J and Schmuttenmaer C A 2018 Tutorial: an introduction to terahertz time domain spectroscopy (THz-TDS) *J. Appl. Phys.* **124** 231101
[33] D'Angelo F, Mics Z, Bonn M and Turchinovich D 2014 Ultra-broadband THz time-domain spectroscopy of common polymers using THz air photonics *Opt. Express* **22** 12475–85
[34] Horng J *et al* 2011 Drude conductivity of Dirac fermions in graphene *Phys. Rev.* B **83** 165113
[35] Maeng I, Lim S, Chae S J, Lee Y H, Choi H and Son J-H 2012 Gate-controlled nonlinear conductivity of dirac fermion in graphene field-effect transistors measured by terahertz time-domain spectroscopy *Nano Lett.* **12** 551–5
[36] Jnawali G, Rao Y, Yan H and Heinz T F 2013 Observation of a transient decrease in terahertz conductivity of single-layer graphene induced by ultrafast optical excitation *Nano Lett.* **13** 524–30
[37] Buron J D *et al* 2015 Terahertz wafer-scale mobility mapping of graphene on insulating substrates without a gate *Opt. Express* **23** 30721–9
[38] Whelan P R *et al* 2019 Non-contact mobility measurements of graphene on silicon carbide *Microelectron. Eng.* **212** 9–12
[39] Mishra N *et al* 2019 Wafer-scale synthesis of graphene on sapphire: toward fab-compatible graphene *Small* **15** 1904906
[40] Whelan P R *et al* 2020 Fermi velocity renormalization in graphene probed by terahertz time-domain spectroscopy *2D Mater.* **7** 035009
[41] Denisultanov A K, Azbite S E, Balbekin N S, Gusev S I and Khodzitsky M K 2014 Optical properties of graphene on quartz and polyethylene substrates in terahertz frequency range *PIERS Proc. (Guangzhou, China)*
[42] Lagatsky A A *et al* 2013 2 μm solid-state laser mode-locked by single-layer graphene *Appl. Phys. Lett.* **102** 013113
[43] Ferrari A C *et al* 2006 Raman spectrum of graphene and graphene layers *Phys. Rev. Lett.* **97** 187401
[44] Ferrari A C and Robertson J 2000 Interpretation of Raman spectra of disordered and amorphous carbon *Phys. Rev.* B **61** 14095–107
[45] Ferrari A C and Basko D M 2013 Raman spectroscopy as a versatile tool for studying the properties of graphene *Nat. Nanotechnol.* **8** 235–46
[46] Bruna M, Ott A K, Ijäs M, Yoon D, Sassi U and Ferrari A C 2014 Doping dependence of the raman spectrum of defected graphene *ACS Nano* **8** 7432–41
[47] Das A *et al* 2008 Monitoring dopants by Raman scattering in an electrochemically top-gated graphene transistor *Nat. Nanotechnol.* **3** 210–5
[48] Basko D M, Piscanec S and Ferrari A C 2009 Electron-electron interactions and doping dependence of the two-phonon Raman intensity in graphene *Phys. Rev.* B **80** 165413
[49] Mohiuddin T M G *et al* 2009 Uniaxial strain in graphene by Raman spectroscopy: G peak splitting, Gr\"uneisen parameters, and sample orientation *Phys. Rev.* B **79** 205433
[50] Zabel J, Nair R R, Ott A, Georgiou T, Geim A K, Novoselov K S and Casiraghi C 2012 Raman spectroscopy of graphene and bilayer under biaxial strain: bubbles and balloons *Nano Lett.* **12** 617–21
[51] Yoon D, Son Y-W and Cheong H 2011 Strain-dependent splitting of the double-resonance Raman scattering band in graphene *Phys. Rev. Lett.* **106** 155502
[52] Proctor J E, Gregoryanz E, Novoselov K S, Lotya M, Coleman J N and Halsall M P 2009 High-pressure Raman spectroscopy of graphene *Phys. Rev.* B **80** 073408
[53] Whelan P R *et al* 2021 Case studies of electrical characterisation of graphene by terahertz time-domain spectroscopy *2D Mater.* **8** 022003
[54] Bøggild P, Mackenzie D M A, Whelan P R, Petersen D H, Buron J D, Zurutuza A, Gallop J, Hao L and Jepsen P U 2017 Mapping the electrical properties of large-area graphene *2D Mater.* **4** 042003
[55] Dawlaty J M, Shivaraman S, Strait J, George P, Chandrashekhar M, Rana F, Spencer M G, Veksler D and Chen Y 2008 Measurement of the optical absorption spectra of epitaxial graphene from terahertz to visible *Appl. Phys. Lett.* **93** 131905
[56] Dai J, Zhang J, Zhang W and Grischkowsky D 2004 Terahertz time-domain spectroscopy characterization of the far-infrared absorption and index of refraction of high-resistivity, float-zone silicon *J. Opt. Soc. Am.* B **21** 1379–86
[57] Glover R E and Tinkham M 1957 Conductivity of superconducting films for photon energies between 0.3 and 40 kT_c *Phys. Rev.* **108** 243–56
[58] Davies C L, Patel J B, Xia C Q, Herz L M and Johnston M B 2018 Temperature-dependent refractive index of quartz at terahertz frequencies *J. Infrared Millim. Terahertz Waves* **39** 1236–48
[59] Whelan P R *et al* 2018 Conductivity mapping of graphene on polymeric films by terahertz time-domain spectroscopy *Opt. Express* **26** 17748–54
[60] Docherty C J and Johnston M B 2012 Terahertz properties of graphene *J. Infrared Millim. Terahertz Waves* **33** 797–815
[61] Bernier M, Garet F and Coutaz J-L 2017 Determining the complex refractive index of materials in the far-infrared from terahertz time-domain data *Terahertz Spectroscopy—A Cutting Edge Technology* (London: IntechOpen) (https://doi.org/10.5772/66348)
[62] Cooper D R *et al* 2012 Experimental review of graphene *ISRN Condens. Matter Phys.* **2012** e501686

[63] Fan X F, Zheng W T, Chihaia V, Shen Z X and Kuo J-L 2012 Interaction between graphene and the surface of SiO_2 *J. Phys.: Condens. Matter Inst. Phys. J.* **24** 305004
[64] Sutter P, Sadowski J T and Sutter E 2009 Graphene on Pt(111): growth and substrate interaction *Phys. Rev.* B **80** 245411
[65] Frank O, Vejpravova J, Holy V, Kavan L and Kalbac M 2014 Interaction between graphene and copper substrate: the role of lattice orientation *Carbon* **68** 440–51
[66] Stauber T, Parida P, Trushin M, Ulybyshev M, Boyda D and Schliemann J 2017 Interacting electrons in graphene: fermi velocity renormalization and optical response *Phys. Rev. Lett.* **118** 266801
[67] Mezzapesa F *et al* 2020 Terahertz frequency combs exploiting an on-chip, solution-processed, graphene-quantum cascade laser coupled-cavity *ACS Photonics* **7** 3489
[68] Reichel K S, Pogna E A A, Biasco S, Viti L, di Gaspare A, Beere H E, Ritchie D A and Vitiello M S 2021 Self-mixing interferometry and near-field nanoscopy in quantum cascade random lasers at terahertz frequencies *Nanophotonics* **10** 1495